Sodium alginate and Chitosan aided design of form-stable Polyrotaxane based phase change materials with ultra-high latent heat

Guang-Zhong Yin, [a, b] Xiao-Mei Yang, [b] Alba Marta López, [b] Mei-Ting Wang, [c] Wen Ye, [b, d, e, f] Baoyun Xu, [d, e] De-Yi Wang [a, b, *]

[a] *Universidad Francisco de Vitoria, Ctra. Pozuelo-Majadahonda Km 1,800, 28223, Pozuelo de Alarcón, Madrid, Spain*

[b] *IMDEA Materials Institute, C/Eric Kandel, 2, 28906 Getafe, Madrid, Spain*

[c] *Liaoning Provincial key Laboratory for Preparation and Application of Special Functional Materials, Shenyang University of Chemical Technology, Shenyang 110142, China*

[d] *Sino-Spanish Joint Research Center for Advanced Materials Technology, Shanghai Research Institute of Chemical Industry Co. LTD., Shanghai, 200062, China*

[e] *Shanghai Engineering Research Center of Functional FR Materials, Shanghai Research Institute of Chemical Industry Co. LTD., Shanghai, 200062, China*

[f] *Universidad Politécnica de Madrid, 28040, Madrid, Spain*

Corresponding Author

*Tel: +34 91 549 34 22, fax: +34 91 550 30 47; Email: deyi.wang@imdea.org

ABSTRACT. We prepared a series of highly porous Polyrotaxane/Sodium alginate, and Polyrotaxane/Chitosan foam alloys according to a sustainable pathway by using water as the only solvent. The foam alloys were further used as supporter materials for Poly (ethylene glycol) (PEG) encapsulation, to fabricate shape-stable bio-based phase change materials (PCMs). The pore morphology and the internal interface between PEG and foam alloys were characterized by scanning electron microscope (SEM). Due to the good compatibility between foam alloys and PEG, the PCM performed perfect anti-leakage properties. The introduction of Sodium alginate or Chitosan ensures the shape stability of the PCMs during the phase transition. The PCMs performed good cycle stability and showed ultra-high latent heat (171.6 J/g -189.5 J/g). Finally, we compared the typical indicators of this work with those reported in the literature, and the comparison highlighted that the present PCMs have the significant advantages: high melting enthalpy, convenient preparation and outstanding sustainability. Notably, the work provided a sustainable idea for the design of anti-leakage and shape-stable PEG-based PCMs.

KEYWORDS: Polyrotaxane, Sodium alginate, Chitosan

Highlights

1. The PCMs have ultra-high latent heat and perfect form stability.

2. The PCM can be fabricated in sustainable process with high efficiency.

3. It expanded the application of Chitosan and Sodium alginate.

1. Introduction

The development of high-performance phase-change materials (PCM) is a practical direction with broad application prospects. With the increasingly prominent "double carbon" and global environmental problems, local governments have proposed corresponding laws and regulations. The development and application of biomass materials and the development of energy-saving and emission-reduction composites are the trend of the era. This will bring the second spring of research on phase change materials, which can be widely used in the building thermal regulation (Saxena et al., 2021, Rathore and Shukla, 2021, Soares et al., 2016) and heat energy storage. (Liu et al., 2022, Kurnia et al., 2022) A typical shape-stable PCM consists of a 3D skeleton and a PCM work substance. (Wang et al., 2022, Li et al., 2022, Xue et al., 2019)

For the 3D skeleton part, more and more scientists have tried various green substrates (such as, Chitosan (CH), (Du et al., 2022, Samoson et al., 2022, Song et al., 2022) Cellulose (Wang et al., 2022, Wu et al., 2022, Zhao et al., 2022) and sodium alginate (SA) (Wang et al., 2022, Zhou et al., 2022)) to prepare 3D-foam for the PCM substance encapsulation. For example, Jia et al. fabricated boron nitride (BN)@chitosan (CH) frameworks with three-dimensional (3D) porous structures were fabricated, and effective thermal conductive pathways could be created in the resultant porous materials for PCM encapsulation.(Jia et al., 2020) Cheng et al. fabricated a flexible supporting material with a folded layer-bridge network structure by dispersing carbon nanotubes (CNTs) in acetic acid solution of CH with poly(vinyl alcohol) (PVA) using a directional freezing method. Then CH/PVA/CNTs scaffold was infiltrated with polyethylene glycol (PEG) to prepare composite PCM. (Cheng et al., 2020) In addition, the PEG was in situ-loaded with Ca^{2+}-crosslinked SA on the account of the coordination of Ca^{2+} with carboxyl groups in the SA structure, to produce the bio-based

composite PCMs.(Liu et al., 2020)

As well reported, phase change thermal storage technology is an effective approach to solving the mismatch between energy supply and demand. However, this technique requires considerable efforts to the successful application and popularization, which required both the high-performance and eco-friendly manufacturing. In view of designing high-performance form-stable PCMs with desirable latent heat enthalpy, in our previous reports, we found the advantages and disadvantages of Polyrotaxane (PLR) supramolecules themselves as phase change materials. (Yin et al., 2021) We achieved the improvement of its function expansion through the further introduction of flame retardants (Yin et al., 2022) and PEG (Yin et al., 2022) to achieve high fire safety or enthalpy optimization of flexible and reprocessable PCM. For further improving the encapsulation ratio of PEG, we envisage that the PLR foam will have a greater absorption potential and the Polyethylene Oxide (PEO) chain of PLR will ensure the perfect compatibility between the foam and the PCM work substance. After brief initial attempts, we found that pure PLR foams tend to collapse during PEG absorption, making it difficult for PCM to retain shape in the end (Figure S1). This may be due to high porosity, imperfect cyclodextrin crystallization, and insufficient physical intersection. In view of the water solubility of PLR, the design principle for the expansion of biomass material functions, we will consider the selection of water-soluble rigid natural macromolecules, such as CH and SA. Both CH and SA could be used as a 3D estimation enhancer to achieve high enthalpy values and good compatibility (structural similarity between cyclodextrins and natural polysaccharides). In summary, this study aimed to design different ratios of PLR/CH, PLR/SA-based alloy foams for the encapsulation of PEG, thereby achieving high enthalpy and high shape stability of the PCMs.

2. Experimental

Materials. Poly (ethylene oxide) (PEO) with a weight average molar mass of 9×10^5 g mol^{-1}, α-Cyclodextrin (α-CD, ≥99.8%) and and sodium alginate (SA, with high viscosity) and PEG 6k were purchased from Sigma Aldrich (USA), Chitosan (CH, 200-600 mPas, was purchased from TCI and used as received. Deionized water is made in our laboratory.

Chitosan solution preparation. The CH solution (3 % (m/v)) was prepared by mixing CH powder as much as 3 grams in 100 mL of distilled water and 2 mL of acetic acid. The solution was stirred for 24 hours.

Sodium Alginate solution preparation. SA has a strong affinity with water and care is required to achieve a homogeneous aqueous solution. The SA solution (3 % (m/v)) was prepared by mixing SA powder as much as 3 grams in 100 mL of distilled water. The solution was stirred using a magnetic stirrer overnight.

Synthesis of Polyrotaxane (PLR). PEO (3 g) was dissolved in H_2O (80 mL) at 80 °C, and then α-CD (1.5 g) with different mass ratio 50% was slowly added. After stirring for overnight at room temperature, the reaction mixture was cooled down and kept at 4 °C for 72 h to yield the corresponding inclusion complex solutions. FTIR (cm^{-1}, KBr window) 3340, 2875, 1645, 1466, 1340, 1278, 1240, 1147, 1096, 1056, 1025, 960, 945, 839, 753, 700, 571. The FTIR curve was provided in Figure S2.

Preparation of foam alloys. The formulations are listed in **Table S1**. We mixed PLR solution with different contents of CH and SA of different contents and freeze-dried.

Characterization. Differential scanning calorimetry (DSC) analysis was performed for each film (5-10 mg) using a TA-Q200 in a N_2 atmosphere (50 mL min^{-1}). Scanning electron microscopy (SEM)

and EDS were carried out on the apparatus (SEM, EVO MA15, Zeiss) and FIB-FEG SEM dual-beam microscope (FIBFESEM) (Helios NanoLab 600i, FEI). Prior to the observation, the conductive gold layer was sprayed. Sample PLR-PA20 was selected for cycle stability test (80 cycles). Both heating and cooling procedures were run at 10 °C min^{-1} to calculate the change of exothermic and endothermic heat as well as the enthalpy efficiency and phase change temperatures. The sample was cut into a disc with a cutter, and then heated at different temperatures (25 °C and 80 °C) for the detecting of form stability (leakage or shape change).

3. Results and discussion

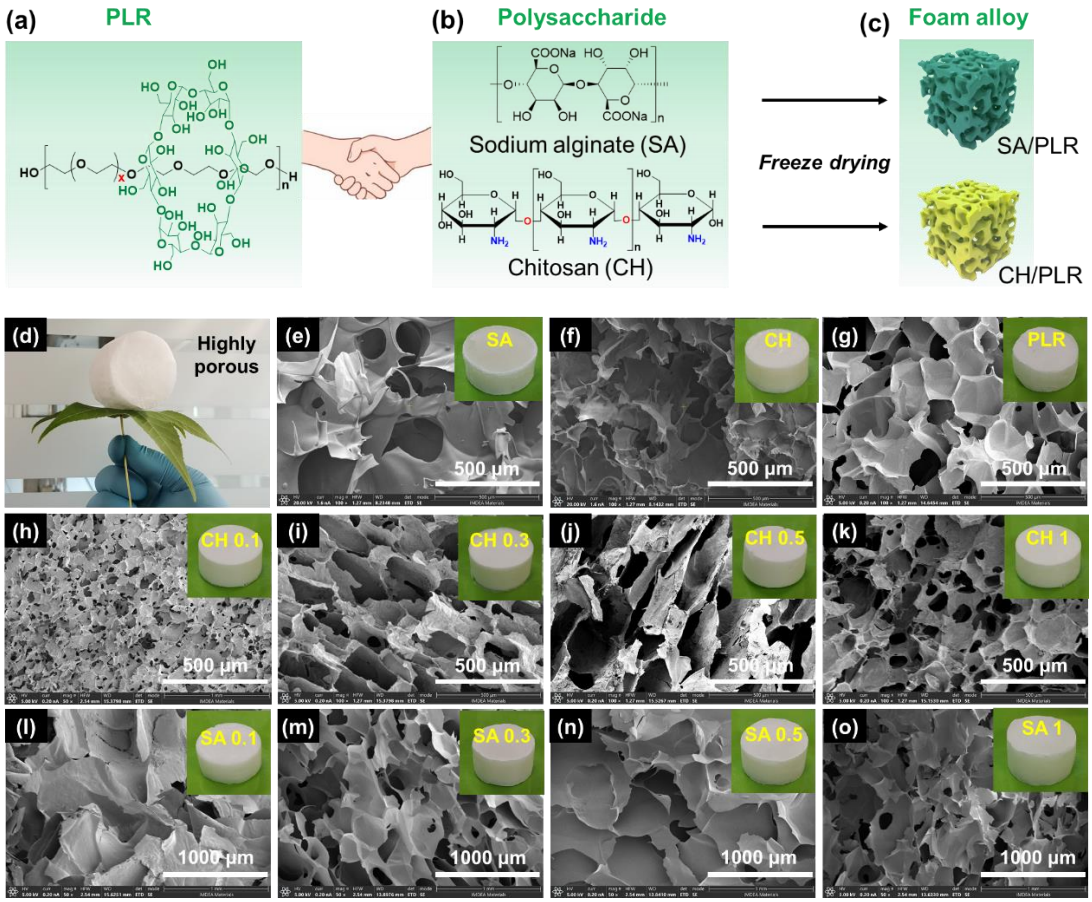

Figure 1. (a) Chemical structure of PLR, (b) Chemical structure of CH and Alginate sodium, (c) illustration of 3D foams (CH-PLR foams and SA-PLR foams), (d) Image of selected foam alloy on the leaf to show the lightweight and highly porous nature of the foam, and SEM images correspond to (e) SA foam, (f) CH foam, (g) PLR foam, (h) CH 0.1, (i) CH 0.3, (j) CH 0.5, (k) CH 1, (l) SA 0.1, (m) SA 0.3, (n) SA 0.5, and (o) SA1.

PLR-50 was prepared according to our previous work, (Yin et al., 2021) and selected as a representative component to blend with different ratio of SA solution (3 wt.%) and CH solution (3 wt.%), respectively (Figure 1a, 1b). After freeze-drying, the foam alloys as shown in Figures 1c and 1d are obtained. The foam alloys were light weight and highly porous, as listed in Table 1. Specific material preparation details (Table S1) were explained in experimental section in the Supplementary materials, and the preparation parameters, porosities were also listed in **Table 1**. Figures 1e-1o show cross-sectional SEM images of all samples. We can see that the pure SA sample has a larger pore size and microscopically shows a larger and connected open pore structure. CH based foams showed a random morphology, with smaller pore sizes than that of SA foam. Pure PLR has more uniform pore structure and has a relative regular wall thickness. PLR-polysaccharide foams exhibited the key characteristics of SA or CH, respectively. Typically, **Figure 1**l-1o still presents a large sheet-like open-pore structure, while for Figure 1h-1k, the pore size is still relatively small. However, the orderliness of the PLR-CH system is improved compared to that of pure CH. Through SEM images, we can also know that the PLR has good compatibility with both SA and CH, which is mainly due to the chemical similarity between α-CD and CH or SA. Accordingly, no phase separation was observed in the SEM section images. The possible reason for this is that PEO and α-CD have structural similarity with polysaccharide and intermolecular hydrogen bonding. Therefore, we believe that the alloy foam is a molecular-level dispersed combination of PLR and CH or SA. This good dispersion will greatly improve the compatibility between the interfaces (PCM substance and supporter), thereby inhibiting the leakage to some extent. In addition, for CH samples, there is a significant shrinkage phenomenon during lyophilization. The porosity of the material can be calculated by Eq. (1). The corresponding data are listed in Table 1. The porosity of the porous

material is measured by Eq (2):(Yin et al., 2016)

$$Porosity\% = \frac{\rho_{bulk}-\rho_{porous}}{\rho_{bulk}} \times 100\% \quad (1)$$

where, $\boldsymbol{\rho_{porous}}$ is the density of porous materials, $\boldsymbol{\rho_{bulk}}$ is the density of bulk polymer and $\boldsymbol{\rho_{PCM}}$ is the density of PCM (after PEG encapsulation). The density values are all calculate and listed in **Table 1**. The efficiency is accordingly calculated and also presented in Table 1.

We can find that the porosities of foam alloys are between 94.65% and 96.47%. Such high porosity can effectively ensure the adsorption and encapsulation efficiency of PCM. The crystallinity (φ_c%) were calculated in the second heating run from 0 °C to 100 °C at heating or cooling rate of 10 °C min^{-1} by Eq. (1):(Yin et al., 2015)

$$\varphi_c\% = \frac{\Delta H_m}{\omega_i \Delta H_m^0} \times 100\% \quad (2)$$

where, ΔH_m (J g^{-1}) represented the measured enthalpies of PCM, ΔH_m^0 (J g^{-1}) was the melting enthalpy for a 100 % crystalline PEG and ω_i was the fraction of the component *i* in the sample. The value taken for ΔH_m^0 of PEG was 196.4 J g^{-1}. (Chrissopoulou et al., 2011) The corresponding $\boldsymbol{\varphi_c}$ **(%)** are summarized in Table 1. All the samples performed ultra-high crystallinity as high as 87.4%~97.6%. We assign that such high crystallinity may originate from the excellent compatibility of foam alloys with PEG.

Table 1. Basic parameters of the foam alloys and the key values of the PCMs

	$\boldsymbol{\rho_{porous}}$ **(g mL^{-1})**	$\boldsymbol{\rho_{bulk}}$ **(g mL^{-1})**	**Porosity (%)**	$\boldsymbol{\rho_{PCM}}$ **(g mL^{-1})**	**Encapsulation efficiency (%)**	**Melting enthalpy (J g^{-1})**	$\boldsymbol{\varphi_c}$ **(%)**
PLR	0.0561±0.0023	1.47±0.04	96.18	-	-	-	-
CH	0.0743±0.0035	0.98±0.03	91.40	1.01±0.04	91.65	178.3	90.78
CH-0.1	0.0597±0.0011	1.44±0.04	95.85	1.22±0.02	95.10	184.7	94.04
CH-0.3	0.0664±0.0019	1.39±0.02	95.21	1.13±0.05	94.12	189.5	96.49
CH-0.5	0.0671±0.0013	1.35±0.07	95.02	1.21±0.06	94.45	187.5	95.47
CH-1	0.0681±0.0043	1.27±0.05	94.65	1.09±0.03	93.75	189.1	96.28
SA	0.0263±0.0052	1.21±0.05	97.83	1.19±0.01	97.79	191.7	97.61
SA-0.1	0.0513±0.0071	1.45±0.04	96.47	1.19±0.03	95.69	187.6	95.52

SA-0.3	0.0531±0.0026	1.43±0.03	96.28	1.13±0.01	95.30	177.6	90.43
SA-0.5	0.0535±0.0013	1.40±0.03	96.19	1.12±0.02	95.22	178.4	90.84
SA-1	0.0569±0.0044	1.37±0.05	95.83	1.14±0.01	95.01	171.6	87.37

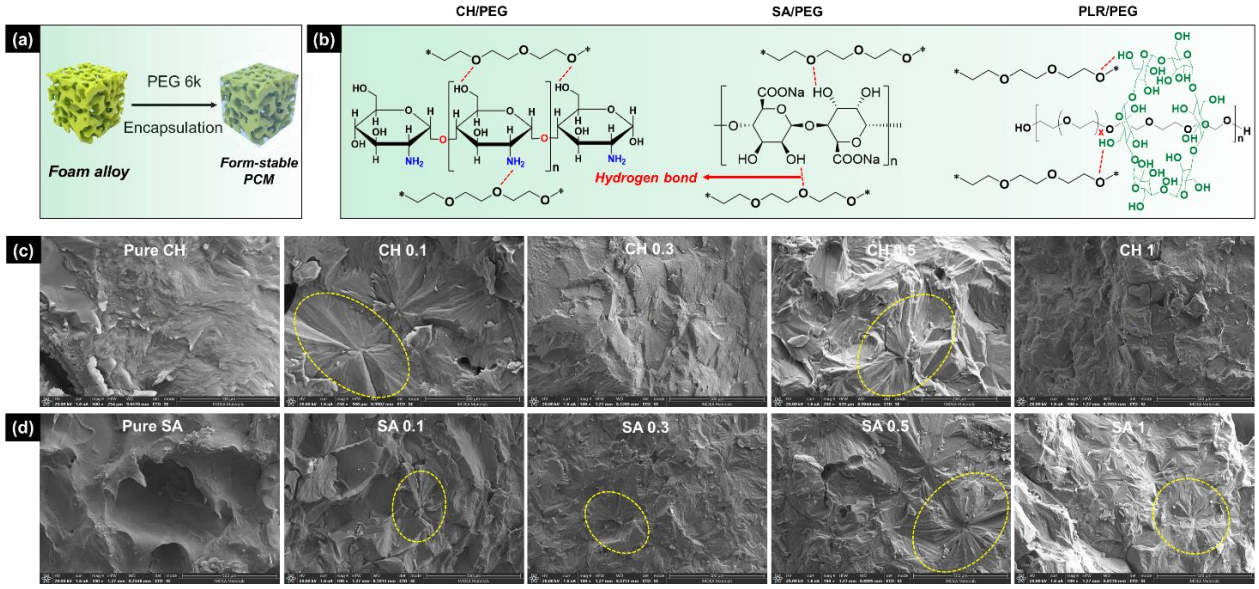

Figure 2. (a) Illustration of the PEG encapsulation process, (b) the potential interaction between PEG and CH, SA and PLR, (c) SEM images of the CH and CH functionalized foam encapsulated PCMs and (d) SEM images of the SA and SA containing foams encapsulated PCM groups.

The foam alloys obtained above was immersed in the melt of PEG6k at 80 ºC in vacuum oven overnight, and finally the form-stable PCMs were obtained. The encapsulation process is shown in Figure 2a. Figure 2b illustrates the potential hydrogen bonding interactions between PEG and CH, SA as well as PLR, due to which, the PEG showed good compatibility with the foam alloy supports. Therefore, no obvious interface delamination was found in the SEM images (Figure 2c and Figure 2d). In addition, we found significant PEG spherulites, indicating that the PEG is inside the alloy foams and can crystalline sufficiently. The observation of many spherulites may be due to the interaction between PEG and the internal micro-nano structures of the foam alloys which easily induce more sufficient PEG crystallization. This is another important factor that increase latent heat. Its specific crystallinity data is calculated according to the Eq. 2 and listed in Table 1. Then, we calculated the specific adsorption amount of PEG and the efficiency of encapsulation by Eq. (3):

$$Encapsulation\ Efficiency\ \% = \frac{m_{PCM} - m_{foam}}{m_{PCM}} \times 100\% = \frac{\rho_{PCM} - \rho_{foam}}{\rho_{PCM}} \times 100\% \qquad (3)$$

where, m_{PCM} and m_{foam} are the weight of the final PCM composited, ρ_{PCM} is the density of the final PCM composites, and ρ_{foam} is the density of the foam.

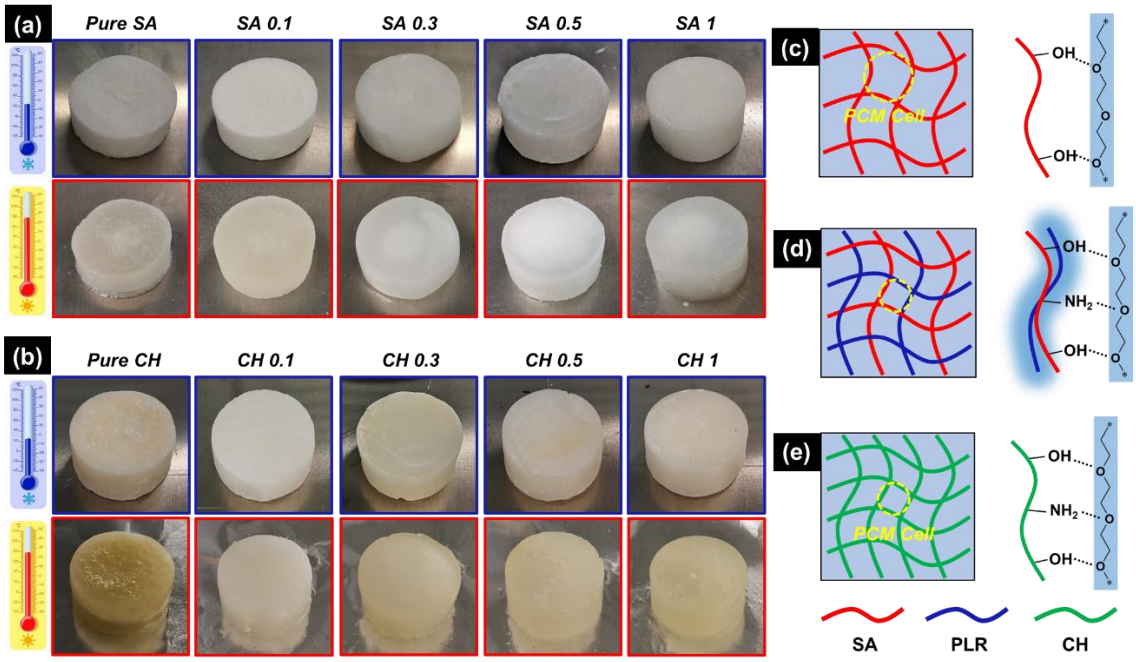

Figure 3. Form stability test of the samples: (a) PLR/SA/PEG group, (b) PLR/CH/PEG group: (blue), 25 °C, (red) 80 °C for 2 h, (c) illustration of micromorphology of pure SA and PEG, (d) PLR/mmm/PEG and (e) illustration of micromorphology of CH/PEG.

As shown in **Figure 3a**, pure SA sample showed slight leakage. The samples containing PLR (SA-0.1 to SA-1) showed no leakage. The pure CH foam does not show significant leakage. It appears more uniform micro pore morphology in the samples with PLR. As for the possible reason for SA encapsulated PCM leakage (as shown in Figure 3c) was assigned that SA foam has a large open pore structure. In addition, in the chemical structure of SA, the hydroxyl density is also relatively low. PEG in the molten state has a large degree of freedom to move in a large internal gap, which is easy to leak accordingly. For CH containing samples, the pore size is small (comparing with SA foam), and the density of polar groups (2 -OH groups and 1 -NH_2) is higher than that of SA (2 -OH groups in one 6-member-ring), so the leakage resistance is better than that of pure SA series

materials (Figure 3e). However, its significant shortcomings are the poor uniformity of pore size and large size shrinkage during molding and freeze drying (Figure 1f) (with about 5~10 % shrinkage in diameter during free drying). In the new samples with PLR, as shown in Figure 3d, the compatibility between the pore wall and PEG substance itself is improved because PLR is compatible with CH or SA in molecular level. Furthermore, because the main molecular chain of PLR is the same as PEG, it can form eutectic, which shows a good space binding effect. Therefore, the leakage resistance has been fully guaranteed and even significantly improved when comparing with the pure SA or pure CH encapsulated samples.

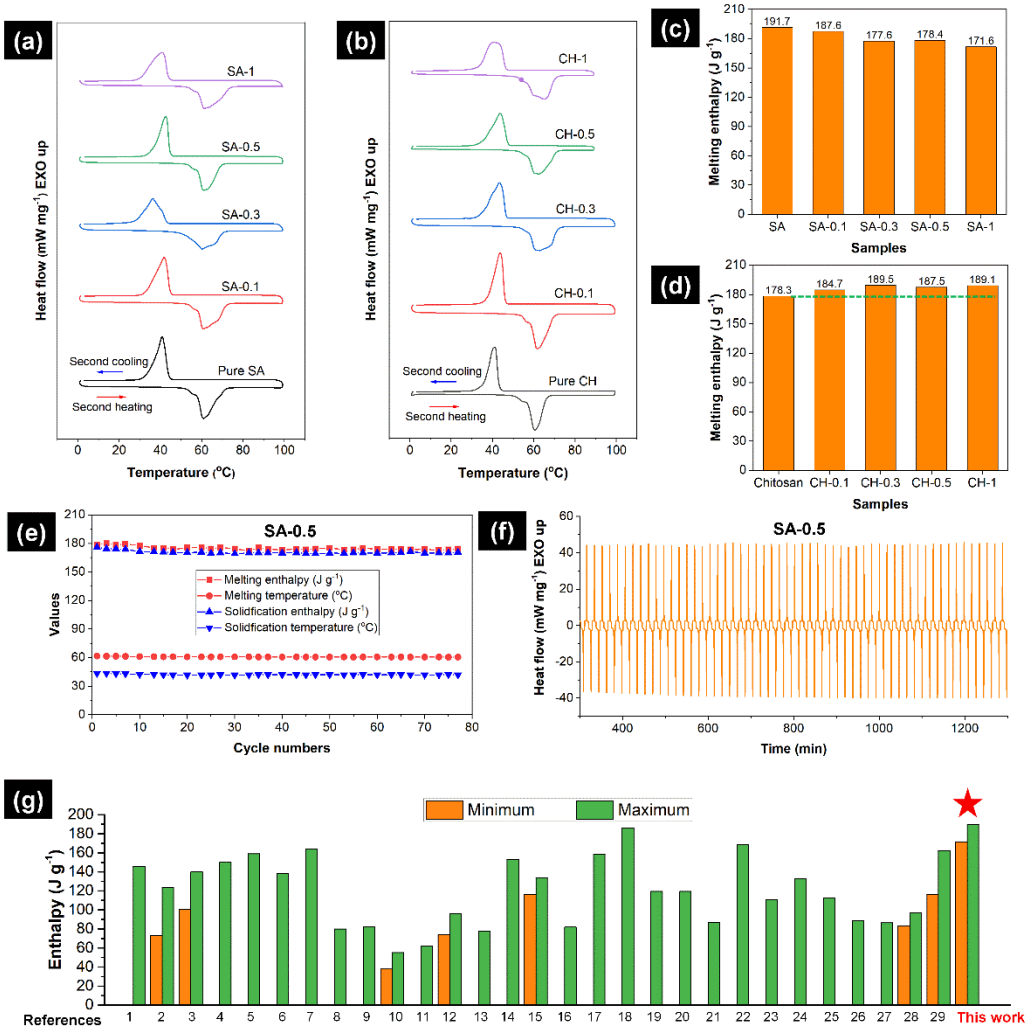

Figure 4. (a) DSC curves of SA-containing PCM samples, (b) DSC curves of CH containing PCMs, (c) latent heat values of the SA-containing PCM samples, (d) latent heat values of the CH-containing PCMs, (e) cycle performance (the main parameters) of the SA-0.5 as a typical example, (f) cycle performance (DSC curves) of sample SA-0.5, and (g) the comparation of latent heat values between the value in current work and the values from literature elsewhere. (The details for reported values were listed in Table 2.)

Figure 4a and 4b show the DSC curves of the SA containing samples and CH containing samples, respectively. We present the latent heat, as shown in **Figure 4**c and 4d. For the SA system, due to the highest porosity and the highest adsorption capacity, it has the highest latent heat (Sample pure SA) with latent heat of 191.75 J g^{-1}. With the addition of PLR, the latent heat decreased due to the change of porosity and micro morphology, but remains at a very high level (higher than 171.6 J g^{-1}). For the CH-containing PCMs, the encapsulation efficiency is relatively low due to the volume shrinkage of the pure CH foam encapsulated samples. After the introduction of the PLR, the porosity increases, so the encapsulation efficiency and enthalpy value also increase. **Figure 4**e and 4f shows the enthalpy value of the material under nearly 80 cycles, and it can be clearly seen that melting temperature, solidification temperature, melting enthalpy and other indicators remain almost constant, indicating that the materials have good cycle stability during phase change. Furthermore, we conduct a series of comparisons with literature reports, and the performance obtained in this work are the highest. As further shown in Table 2, the recently reported latent heat of phase transition of PEG-based PCM is generally below 160 J g^{-1}. The supporting materials used are mostly petroleum-based compounds; (Shi et al., 2022) (Du et al., 2021) organic solvents are sometimes involved in the preparation process;(Li et al., 2022, Tian et al., 2022) which increase the environmental cost to some extent. In addition, in some reports, the authors directly used inorganic 3D foam as the support materials, (Li and Wang, 2021, Liu et al., 2021) which maybe increase the possibility of leakage due to the difference in interfacial compatibility between PEG and the

inorganic micro-nano structure. By the comparation analysis, we claim that the process is simple and environmentally friendly, so it is a sustainable material research system. The comparison shows that this work has the following significant advantages: (1) high melting enthalpy, (2) convenient preparation and outstanding sustainability.

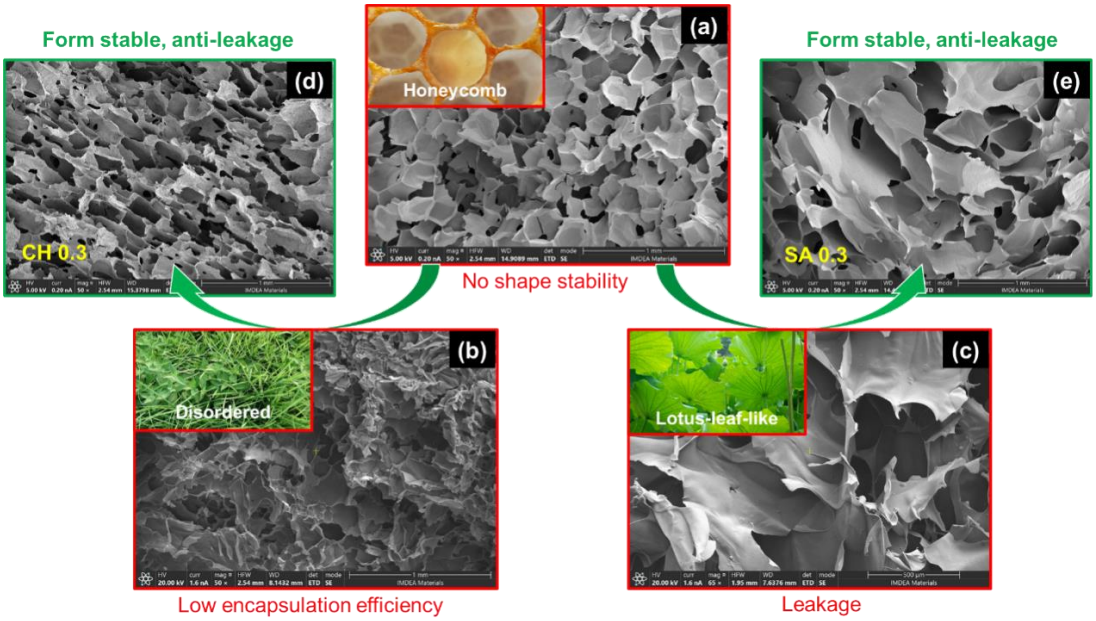

Figure 5 (a) Honeycomb like PLR foam, (b) discorded pore structure of CH foam, (c) Lotus-leaf-like structure of SA foam, (d) SEM image of sample with both CH and PLR, and (e) the SEM image of sample with both SA and PLR.

We know that all the PLR, CH and SA have specific deficiencies in the preparation of foam-encapsulated PEG (**Figure 5**). For example, the Honeycomb-shaped PLR foam (Figure 5a) collapsed during the adsorption process, the foam volume shrinks significantly during the freeze drying of CH foam with low porosity (Figure 5b) accordingly, while the large-pore foam formed by SA (Figure 5c) showed significant leakage during the phase transition process. Fortunately, high-performance encapsulation of PEG can be achieved by blending Polyrotaxane with SA or CH to prepare foam alloys (Figure 5d and 5e). Through comparative analysis, we realized that in the material system, the PLR and the polysaccharide double network in the alloy foams each act as

different functional components. The Polyrotaxane optimizes the compatibility of the foam cell surface with PEG, and the polysaccharide acts as the stereotyped backbone. Therefore, overall, the double network alloy systems have excellent comprehensive properties. Moreover, the application and promotion of natural macromolecules is in line with the needs of the era of sustainable development.

Table 2. Comparison with the preparation method, key parameters for the PEG based PCMs in the literature elsewhere.

No.	Supporter materials	PCM substance	Preparation method	Solvent used	PEG loading rate (%)	Enthalpy efficiency (%)	Latent heat ($J\ g^{-1}$)	References
1	Chemically cross-linked cellulose nanocrystal	PEG-4000	In-situ synthesis	Water	85.7	95.0	145.8	(Cheng et al., 2022)
2	π-π stacking	PEG-4000	Block copolymerization	Tetrahydrofuran	-	-	72.8-123.4	(Tian et al., 2022)
3	Potatoes/MXene	PEG-6000	Vacuum impregnation	Water	-	91.5-98.3	100.5-139.9	(Fang et al., 2022)
4	Polyimide (PI)/phosphorene (PR) hybrid aerogel	PEG-6000	Vacuum impregnation	-	90.0	97.0	150.0	(Shi et al., 2022)
5	Graphene/cysteamine aerogel	PEG-6000	Vacuum impregnation	Water	98.2	-	159.0	(Yu et al., 2022)
6	Poly(acrylamide-co-acrylic acid) copolymer	PEG-6000	Free radical polymerization	NaOH	89.0	96.1	138.6	(Yang et al., 2022)
7	Polyvinyl alcohol	PEG-2000	Vacuum immersion	boric acid/ APP/BN/water	93.0	91.1	163.9	(Zhou et al., 2022)
8	Boron nitride (BN) and Expanded graphite and EP	PEG-4000	Blending and curing	-	54.0	75.1	79.9	(Luo et al., 2022)
9	Halloysite-based FSPCM	PEG-1000	Encapsulate	H_2SO_4 and water	55.0	95.8	82.2	(Gu et al., 2022)
10	Expanded vermiculite/−boron nitride	PEG 2k	typical vacuum impregnation	EtOH	88.0-97.0	-	37.8-55.3	(Wang et al., 2022)
11	Carbon fibers and polyacrylic acid	PEG-2000	Freeze casting technology	N,N'-methylenebis (acryl-amide)	-	-	62.0	(Li et al., 2022)

12	Polyethylene glycol (PEG)/epoxy (EP) resin	PEG-6000	Curing reaction	-	50.0-80.0	-	74.0-96.1	(Wang et al., 2022)
13	Mica	PEG-1000	Vacuum impregnation	-	86.0	98.5	77.7	(Zhang et al., 2022)
14	3D porous TiO_2	PEG-6000	Physical impregnation	Water/EtOH	92.0	93.3	153.3	(Sun et al., 2021)
15	SiO_2 network and MWCNTs-COOH	PEG-6000	Sol-gel method	Water	81.0-84.4	-	116.3-133.5	(Yan et al., 2021)
16	Mesoporous carbon FDU-15	PEG	Melting impregnation	EtOH	75.0	71.3	81.8	(Feng et al., 2021)
17	3D metal–organic network	PEG-20000	Hydrogen bonding interaction	Water	98.0	99.0	158.4	(Wang et al., 2021)
18	Melamine foam and MXene	PEF-4000	Vacuum impregnation	Water	98.3	101.3	186.2	(Du et al., 2021)
19	Rice husk ash	PEG-2000	Physical mixing and impregnation process	-	-	-	119.3	(Yu et al., 2021)
20	Nanoporous fumed silica	PEG-2000	Melt spinning technique	EtOH	-	-	119.4	(Xia et al., 2021)
21	Poly (Glycerol-Itaconic acid)	PEG-6000	Polycondensation + BPO curing	-	72.7	67.9	86.9	(Yin et al., 2021)
22	Lignin-modified graphene aerogel	PEG-4000	Vacuum impregnation	Water/EtOH	99.2	98.4	168.7	(Wei et al., 2021)
23	Expanded vermiculite composite	PEG	Physical blending and impregnation	-	-	-	110.7	(Deng, 2021)
24	Chemically treated wood	PEG-4000	Vacuum impregnation	$NaOH/Na_2SO_3$	-	99.7	132.6	(Liu et al., 2021)
25	Bio-based bamboo flour	PEG-10000	Straightforward dry ball milling	-	70.0	61.1	113.0	(Zheng et al., 2022)
26	Bionic hierarchical porous aluminum nitride ceramic	PEG 2k	-	Water	42.9	-	88.7	(Qiu et al., 2021)
27	Azobenzene-Graphene	PEG	Ultrasound-assisted physically blended	-	95.0	-	86.5	(Li and Wang, 2021)
28	MXene	PEG-6000	Vacuum curing process	-	70.0-90.0		83.3-96.8	(Liu et al., 2021)
29	PLR	PEG	Solvent casting	Water	<77.8	>100	116.1-162.2	(Yin et al., 2022)
30	PLR-P foam alloy	PEG	3D foam encapsulation	Water	-	87.4-96.3	171.6-189.5	Current work

4. Conclusions

In order to prepare high-performance 3D form-stable PCM, two kinds of polysaccharides, CH and SA were used in this work to modify the form stability of PLR based foam. By adjusting the ratio of PLR to polysaccharides, the pore size and morphology can be regulated. The resulting foams have high porosity (>94.65 %) and high PEG uptake (93.75 %), resulting in the high phase transition enthalpies of 171.6-189.5 J g^{-1}. The PCMs showed outstanding form stability and leakage resistance. In the process, we are gratifying to find that while improving the shape stability of Polyrotaxane by compounding polysaccharides, Polyrotaxane also effectively regulates the practical problems, namely, the leakage of SA foam and the volume shrinkage of CH foam. Specifically, Polyrotaxane acts as host and compatibilizer with PEG for ensuring the anti-leakage performance, while SA and CH act as dimensional stabilizers to keep the 3D stable shape. Notably, the preparation convenience and the sustainability of materials, and the outstanding performance indicators of PCM are expected to be practically popularized and applied in the field of phase change energy storage. Moreover, the current system mainly investigated the effect of foam alloy components on the latent heat and the encapsulation rate of PCM work substance. We will consider further improvement of comprehensive properties based on the currently optimal composition. Typically, thermal conductivity and fire safety will be the focus of the next step.

Declaration of Competing Interest

The authors declare that they have no known competing financial interests or personal relationships that could have appeared to influence the work reported in this paper.

CRediT authorship contribution statement

Guang-Zhong Yin: Conceptualization, Methodology, Validation, Data curation, Writing-original draft, Writing-review & editing, Project administration. **Xiao-Mei Yang**: Validation, Data curation, Writing-original draft, Writing-review & editing. **Alba Marta López**: Data curation, Investigation, Writing-review & editing. **Mei-Ting Wang**: Formal analysis, Writing-review & editing. **Wen Ye**: Formal analysis, Writing-review & editing. **Baoyun Xu**: Formal analysis, Writing-review & editing. **De-Yi Wang**: Project administration, Methodology, Writing-review & editing, Supervision, Funding acquisition.

Acknowledgment

The authors acknowledge the financial support provided by BIOFIRESAFE Project funded by Ministerio De Ciencia E Innovación (MINECO), Spain with Project number: PID2020-117274RB-I00BIOFIRESAFE.

References

Saxena, R., S. F. Ali and D. Rakshit, 14 - PCM incorporated bricks: A passive alternative for thermal regulation and energy conservation in buildings for Indian conditions. *Eco-efficient Materials for Reducing Cooling Needs in Buildings and Construction* **2021**, 303-328.

Rathore, P. K. S. and S. K. Shukla, 2021. Enhanced thermophysical properties of organic PCM through shape stabilization for thermal energy storage in buildings: A state of the art review. Energy and Buildings 236, 110799. https://doi.org/10.1016/j.enbuild.2021.110799.

Soares, N., A. R. Gaspar, P. Santos and J. J. Costa, 2016. Experimental evaluation of the heat transfer through small PCM-based thermal energy storage units for building applications. Energy and Buildings 116, 18-34. https://doi.org/10.1016/j.enbuild.2016.01.003.

Liu, X., F. Yang, M. Li, C. Sun and Y. Wu, 2022. Development of cost-effective PCM-carbon foam composites for thermal energy storage. Energy Reports 8, 1696-1703. https://doi.org/10.1016/j.egyr.2021.12.065.

Kurnia, J. C., L. A. F. Haryoko, I. Taufiqurrahman, L. Chen, L. Jiang and A. P. Sasmito, 2022. Optimization of an innovative hybrid thermal energy storage with phase change material (PCM) wall insulator utilizing Taguchi method. Journal of Energy Storage 49, 104067. https://doi.org/10.1016/j.est.2022.104067.

Wang, J., M. Shen, Z. Liu and W. Wang, 2022. MXene materials for advanced thermal management and thermal energy utilization. Nano Energy 97, 107177. https://doi.org/10.1016/j.nanoen.2022.107177.

Li, W., D. Zhai, Y. Gu, Y. Cao, L. Zhang, X. Sheng and Y. Chen, 2022. 3D zirconium phosphate/polyvinyl alcohol composite aerogels for form-stable phase change materials with brilliant thermal energy storage

capability. Solar Energy Materials and Solar Cells 239, 111681. https://doi.org/10.1016/j.solmat.2022.111681.

Xue, F., Y. Lu, X.-d. Qi, J.-h. Yang and Y. Wang, 2019. Melamine foam-templated graphene nanoplatelet framework toward phase change materials with multiple energy conversion abilities. Chemical Engineering Journal 365, 20-29. https://doi.org/10.1016/j.cej.2019.02.023.

Du, G., X. Lai, J. Hu and Z. Zhang, 2022. Construction of high thermal conductive boron Nitrid@Chitosan aerogel/ paraffin composite phase change material. Solar Energy Materials and Solar Cells 240, 111532. https://doi.org/10.1016/j.solmat.2021.111532.

Samoson, K., A. Soleh, K. Saisahas, K. Promsuwan, J. Saichanapan, P. Kanatharana, P. Thavarungkul, K. H. Chang, A. F. Lim Abdullah, K. Tayayuth and W. Limbut, 2022. Facile fabrication of a flexible laser induced gold nanoparticle/chitosan/ porous graphene electrode for uric acid detection. Talanta 243, 123319. https://doi.org/10.1016/j.talanta.2022.123319.

Song, W., Q. Zhang, Y. Guan, W. Li, S. Xie, J. Tong, M. Li and L. Ren, 2022. Synthesis and Characterization of Porous Chitosan/Saccharomycetes Adsorption Microspheres. Polymers 14 (11), 2292.

Wang, Q., Z. Gao and Y. Xiong, 2022. Cellulose/Ag-MWCNT/MXene composite scaffolds with hierarchical pores and fast light-to-heat conversion for the preparation of shape-stable phase change materials for thermal energy storage. Journal of Materials Science 57 (3), 1962-1976. 10.1007/s10853-021-06659-7.

Wu, G., N. Bing, Y. Li, H. Xie and W. Yu, 2022. Three-dimensional directional cellulose-based carbon aerogels composite phase change materials with enhanced broadband absorption for light-thermal-electric conversion. Energy Conversion and Management 256, 115361. https://doi.org/10.1016/j.enconman.2022.115361.

Zhao, L., G. Yang, C. Shen, Z. Mao, B. Wang, X. Sui and X. Feng, 2022. Dual-functional phase change composite based on copper plated cellulose aerogel. Composites Science and Technology 227, 109615. https://doi.org/10.1016/j.compscitech.2022.109615.

Wang, W., M. Fan, J. Ni, W. Peng, Y. Cao, H. Li, Y. Huang, G. Fan, Y. Zhao and S. Song, 2022. Efficient dye removal using fixed-bed process based on porous montmorillonite nanosheet/poly(acrylamide-co-acrylic acid)/sodium alginate hydrogel beads. Applied Clay Science 219, 106443. https://doi.org/10.1016/j.clay.2022.106443.

Zhou, J., G. Du, J. Hu, X. Lai, S. Liu and Z. Zhang, 2022. The establishment of Boron nitride @sodium alginate foam/ polyethyleneglycol composite phase change materials with high thermal conductivity, shape stability, and reusability. Chinese Journal of Chemical Engineering, https://doi.org/10.1016/j.cjche.2022.04.001.

Jia, X., Q. Li, C. Ao, R. Hu, T. Xia, Z. Xue, Q. Wang, X. Deng, W. Zhang and C. Lu, 2020. High thermal conductive shape-stabilized phase change materials of polyethylene glycol/boron nitride@chitosan composites for thermal energy storage. Composites Part A: Applied Science and Manufacturing 129, 105710. https://doi.org/10.1016/j.compositesa.2019.105710.

Cheng, P., H. Gao, X. Chen, Y. Chen, M. Han, L. Xing, P. Liu and G. Wang, 2020. Flexible monolithic phase change material based on carbon nanotubes/chitosan/poly(vinyl alcohol). Chemical Engineering Journal 397, 125330. https://doi.org/10.1016/j.cej.2020.125330.

Liu, L., X. Fan, Y. Zhang, S. Zhang, W. Wang, X. Jin and B. Tang, 2020. Novel bio-based phase change materials with high enthalpy for thermal energy storage. Applied Energy 268, 114979. https://doi.org/10.1016/j.apenergy.2020.114979.

Yin, G.-Z., J. Hobson, Y. Duan and D.-Y. Wang, 2021. Polyrotaxane: New generation of sustainable,

ultra-flexible, form-stable and smart phase change materials. Energy Storage Materials 40, 347-357. https://doi.org/10.1016/j.ensm.2021.05.023.

Yin, G.-Z., A. Marta López, X.-M. Yang, W. Ye, B. Xu, J. Hobson and D.-Y. Wang, 2022. Shape-stable and Smart Polyrotaxane-based Phase Change Materials with Enhanced Flexibility and Fire-safety. European Polymer Journal, 111262. https://doi.org/10.1016/j.eurpolymj.2022.111262.

Yin, G.-Z., A. Marta López, X.-M. Yang, X. Ao, J. Hobson and D.-Y. Wang, 2022. Polyrotaxane based leakage-proof and injectable phase change materials with high melting enthalpy and adjustable transition temperature. Chemical Engineering Journal 444, 136421. https://doi.org/10.1016/j.cej.2022.136421.

Yin, G., D. Zhao, Y. Ren, L. Zhang, Z. Zhou and Q. Li, 2016. A convenient process to fabricate gelatin modified porous PLLA materials with high hydrophilicity and strength. Biomaterials Science 4 (2), 310-318. 10.1039/C5BM00414D.

Yin, G., D. Zhao, X. Wang, Y. Ren, L. Zhang, X. Wu, S. Nie and Q. Li, 2015. Bio-compatible poly(ester-urethane)s based on PEG-PCL-PLLA copolymer with tunable crystallization and bio-degradation properties. RSC Advances 5 (96), 79070-79080. 10.1039/C5RA15531B.

Chrissopoulou, K., K. S. Andrikopoulos, S. Fotiadou, S. Bollas, C. Karageorgaki, D. Christofilos, G. A. Voyiatzis and S. H. Anastasiadis, 2011. Crystallinity and Chain Conformation in PEO/Layered Silicate Nanocomposites. Macromolecules 44 (24), 9710-9722. 10.1021/ma201711r.

Shi, T., Z. Zheng, H. Liu, D. Wu and X. Wang, 2022. Flexible and foldable composite films based on polyimide/phosphorene hybrid aerogel and phase change material for infrared stealth and thermal camouflage. Composites Science and Technology 217, 109127. https://doi.org/10.1016/j.compscitech.2021.109127.

Du, Y., H. Huang, X. Hu, S. Liu, X. Sheng, X. Li, X. Lu and J. Qu, 2021. Melamine foam/polyethylene glycol composite phase change material synergistically modified by polydopamine/MXene with enhanced solar-to-thermal conversion. Renewable Energy 171, 1-10. https://doi.org/10.1016/j.renene.2021.02.077.

Li, M., L. Li, Y. Qin, X. Wei, X. Kong, Z. Zhang, S. Xiong, H. Do, J. C. Greer, Z. Pan, T. Cai, W. Dai, C.-T. Lin, N. Jiang and J. Yu, 2022. Crystallization induced realignment of carbon fibers in a phase change material to achieve exceptional thermal transportation properties. Journal of Materials Chemistry A 10 (2), 593-601. 10.1039/D1TA09056A.

Tian, C., J. Ning, Y. Yang, F. Zeng, L. Huang, Q. Liu, J. Lv, F. Zhao, W. Kong and X. Cai, 2022. Super tough and stable solid–solid phase change material based on π-π stacking. Chemical Engineering Journal 429, 132447. https://doi.org/10.1016/j.cej.2021.132447.

Li, M. and C. Wang, 2021. AAZO-Graphene composite phase change materials with Photo-thermal conversion performance. Solar Energy 223, 11-18. https://doi.org/10.1016/j.solener.2021.05.036.

Liu, H., R. Fu, X. Su, B. Wu, H. Wang, Y. Xu and X. Liu, 2021. MXene confined in shape-stabilized phase change material combining enhanced electromagnetic interference shielding and thermal management capability. Composites Science and Technology 210, 108835. https://doi.org/10.1016/j.compscitech.2021.108835.

Cheng, M., J. Hu, J. Xia, Q. Liu, T. Wei, Y. Ling, W. Li and B. Liu, 2022. One-step in-situ green synthesis of cellulose nanocrystal aerogel based shape stable phase change material. Chemical Engineering Journal 431, 133935. https://doi.org/10.1016/j.cej.2021.133935.

Fang, Y., S. Liu, X. Li, X. Hu, H. Wu, X. Lu and J. Qu, 2022. Biomass porous potatoes/MXene encapsulated PEG-based PCMs with improved photo-to-thermal conversion capability. Solar Energy Materials and Solar Cells 237, 111559. https://doi.org/10.1016/j.solmat.2021.111559.

Yu, C., J. Park, J. Ryoun Youn and Y. Seok Song, 2022. Integration of form-stable phase change material into pyroelectric energy harvesting system. Applied Energy 307, 118212. https://doi.org/10.1016/j.apenergy.2021.118212.

Yang, H., Y. Bai, C. Ge, L. He, W. Liang and X. Zhang, 2022. Polyethylene glycol-based phase change materials with high photothermal conversion efficiency and shape stability in an aqueous environment for solar water heater. Composites Part A: Applied Science and Manufacturing 154, 106778. https://doi.org/10.1016/j.compositesa.2021.106778.

Zhou, M., D. Xie, K. Zhou, K. Gong, L. Yin, X. Qian and C. Shi, 2022. 3D porous aerogel based-phase change materials with excellent flame retardancy and shape stability for both thermal and light energy storage. Solar Energy Materials and Solar Cells 236, 111537. https://doi.org/10.1016/j.solmat.2021.111537.

Luo, F., Y. He, W. Cui, Y. Guo, Y. Jin, H. Li, B. Huang and Q. Qian, 2022. Shape-Stabilized Phase Change Materials with Superior Thermal Conductivity for Thermal Energy Harvesting. ACS Applied Polymer Materials 4 (3), 2160-2168. 10.1021/acsapm.2c00105.

Gu, X., L. Peng, P. Liu, L. Bian and B. Wei, 2022. Enhanced thermal properties and lab-scale thermal performance of polyethylene glycol/modified halloysite nanotube form-stable phase change material cement panel. Construction and Building Materials 323, 126550. https://doi.org/10.1016/j.conbuildmat.2022.126550.

Wang, H., J. Lei, T. Wu, D. Wu, H. Liu, Y. Deng and F. Wu, 2022. Effect of Boron Nitride on the Heat Transfer and Heat Storage of Poly(ethylene glycol)/Expanded Vermiculite Composite Phase-Change Materials. ACS Omega 7 (2), 2438-2443. 10.1021/acsomega.1c06502.

Wang, T., C. Wang, K. Chen, X. Liu and Z. Huang, 2022. Preparation, thermal, and mechanical properties of polyethylene glycol/expoxy resin composites as form-stable phase change materials. Polymer Engineering & Science 62 (2), 520-529. https://doi.org/10.1002/pen.25864.

Zhang, D., C. Li, N. Lin, B. Xie and J. Chen, 2022. Mica-stabilized polyethylene glycol composite phase change materials for thermal energy storage. International Journal of Minerals, Metallurgy and Materials 29 (1), 168-176. 10.1007/s12613-021-2357-4.

Sun, X., M. Yi, B. Feng, R. Liu, L. Sun, L. Zhai, H. Cao and C. Zou, 2021. Shape-stabilized composite phase change material PEG@TiO2 through in situ encapsulation of PEG into 3D nanoporous TiO2 for thermal energy storage. Renewable Energy 170, 27-37. https://doi.org/10.1016/j.renene.2021.01.114.

Yan, D., W. Ming, S. Liu, G. Yin, Y. Zhang, B. Tang and S. Zhang, 2021. Polyethylene glycol (PEG)/silicon dioxide grafted aminopropyl group and carboxylic multi-walled carbon nanotubes (SAM) composite as phase change material for light-to-heat energy conversion and storage. Journal of Energy Storage 36, 102428. https://doi.org/10.1016/j.est.2021.102428.

Feng, D., P. Li, Y. Feng, Y. Yan and X. Zhang, 2021. Using mesoporous carbon to pack polyethylene glycol as a shape-stabilized phase change material with excellent energy storage capacity and thermal conductivity. Microporous and Mesoporous Materials 310, 110631. https://doi.org/10.1016/j.micromeso.2020.110631.

Wang, R., Q. Li, G. Du, P. He, L. Xu, G. Liang, L. Bao and Y. Xiao, 2021. A hydrogel-like form-stable phase change material with high loading efficiency supported by a three dimensional metal–organic network. Chemical Engineering Journal 420, 129898. https://doi.org/10.1016/j.cej.2021.129898.

Yu, K., Y. Liu and Y. Yang, 2021. Enhanced thermal properties of polyethylene glycol/modified rice husk ash eco-friendly form-stable phase change material via optimizing support pore structure. Journal of Energy Storage 43, 103172. https://doi.org/10.1016/j.est.2021.103172.

Xia, W., H. Xiang, Z. Zhou, X. Fei and M. Zhu, 2021. Hybridizing rational designed hydrophobic PEG-based derivatives into nanoporous F–SiO2 as form-stable phase change materials for melt-spun PA6 phase change fibers with a superior washing durability. Composites Communications 24, 100633. https://doi.org/10.1016/j.coco.2021.100633.

Yin, G.-Z., J. L. Díaz Palencia and D.-Y. Wang, 2021. Fully bio-based Poly (Glycerol-Itaconic acid) as supporter for PEG based form stable phase change materials. Composites Communications 27, 100893. https://doi.org/10.1016/j.coco.2021.100893.

Wei, D., C. Wu, G. Jiang, X. Sheng and Y. Xie, 2021. Lignin-assisted construction of well-defined 3D graphene aerogel/PEG form-stable phase change composites towards efficient solar thermal energy storage. Solar Energy Materials and Solar Cells 224, 111013. https://doi.org/10.1016/j.solmat.2021.111013.

Deng, Y., 2021. Effect of Ag nanowires on crystallization behavior of polyethylene glycol/expanded vermiculite composite phase change material. Journal of Energy Storage 34, 102223. https://doi.org/10.1016/j.est.2020.102223.

Liu, S., H. Wu, Y. Du, X. Lu and J. Qu, 2021. Shape-stable composite phase change materials encapsulated by bio-based balsa wood for thermal energy storage. Solar Energy Materials and Solar Cells 230, 111187. https://doi.org/10.1016/j.solmat.2021.111187.

Zheng, C., H. Zhang, L. Xu and F. Xu, 2022. Production of multifunctional bamboo-based phase change encapsulating material by straightforward dry ball milling. Journal of Energy Storage 46, 103630. https://doi.org/10.1016/j.est.2021.103630.

Qiu, L., K. Yan, Y. Feng, X. Liu and X. Zhang, 2021. Bionic hierarchical porous aluminum nitride ceramic composite phase change material with excellent heat transfer and storage performance. Composites Communications 27, 100892. https://doi.org/10.1016/j.coco.2021.100892.